LAWRENCE
LIVERMORE
NATIONAL
LABORATORY

LLNL-JRNL-582197

Ab-initio calculation of optical properties of wurtzitic In_x Ga_1x N and In_x Al_1x N alloys including excitonic effects

L. C. de Carvalho, A. Schleife, J. Furthmueller, F. Bechstedt

September 17, 2012

Physical Review B

Disclaimer

Ab-initio calculation of optical properties of wurtzitic $In_xGa_{1-x}N$ and $In_xAl_{1-x}N$ alloys including excitonic effects

Luiz Cláudio de Carvalho,[1,2,*] André Schleife,[2,3] Jürgen Furthmüller,[1,2] and Friedhelm Bechstedt[1,2]

[1]*Institut für Festkörpertheorie und -optik, Friedrich-Schiller-Universität, Max-Wien-Platz 1, 07743 Jena, Germany*
[2]*European Theoretical Spectroscopy Facility (ETSF)*
[3]*Condensed Matter and Materials Division, Lawrence Livermore National Laboratory, Livermore, California 94550, USA*

(Dated: September 10, 2012)

By combining modern many-body approaches with a cluster expansion scheme, frequency-dependent dielectric functions including excitonic and local-field effects are computed for wurtzitic group-III nitride alloys with varying composition *x*. The quasiparticle electronic structure required to construct the quasielectron-quasihole pair Hamiltonian for each cluster is approximated using a LDA+*U*+Δ approach. Two different cluster statistics are employed to perform configurational averages for the frequency-dependent complex dielectric function. Comparing the resulting composition dependence of peak positions and intensities to experimental data allows conclusions regarding the distribution of the group-III cations in the alloys.

PACS numbers: 71.35.Cc, 78.20.Bh, 78.20.Ci, 78.40.Fy, 78.66.Fd
Keywords: parameter-free calculations, nitride semiconductor alloys, optical properties, excitons, cluster expansion, dielectric constants

I. INTRODUCTION

The group-III nitrides InN, GaN, and AlN have received considerable attention for high-power, high-frequency, and high-temperature electronic devices and, in particular, for optoelectronic applications such as light-emitting and laser diodes.[1] Indeed, current advances in solid-state lighting are driven by tailoring of ternary nitrides, e.g. $In_xGa_{1-x}N$ and $In_xAl_{1-x}N$ alloys. The binary nitrides crystallize in the wurtzite (*wz*) structure and show a dipole-allowed lowest direct optical transition. The fundamental band gaps of these materials vary between 0.7 eV (InN[2,3]), 3.5 eV (GaN[4]), and 6.2 eV (AlN[4]). Therefore, absorption and emission edges of their alloys may cover the electromagnetic spectrum from the infrared to the ultraviolet.

However, the growth of almost defect-free and homogeneous $In_xGa_{1-x}N$ and $In_xAl_{1-x}N$ samples is still a challenge for compositions *x* that deviate significantly from the binary end components. The alloys resulting from different growth experiments have been discussed controversially in the literature (see Ref. 5 and references therein). Still a deeper understanding of the distribution of the cations in the alloy samples and the impact of the preparation conditions is needed and spectroscopic studies of the alloys in a wide energy range may contribute to such an understanding. Indeed, for technologically highly important alloys of hexagonal group-III nitrides such as $In_xGa_{1-x}N$,[6–8] $In_xAl_{1-x}N$,[9,10] and $Al_xGa_{1-x}N$[11] spectroscopic ellipsometry measurements of the optical properties across a wide spectral range exist. The variation of the line shape, peak positions, and intensities of the absorption spectra with composition *x* allows deep insight into the distribution of the group-III cations on their sublattice, the strength of composition fluctuations, and the appearance of clustering phenomena (see Refs. 5 and 12 and references therein). The interpretation of these spectra is, however, not always easy and strongly benefits from the comparison to theoretical results that account for many-body effects[13–15] as well as a reasonable description of the alloying.[5,16,17] However, converged calculations of optical properties are still a challenge and have been carried out for alloys only in a very few cases of oxides.[17]

In the last decade enormous progress has been made in the *ab-initio* description of optical properties of bulk semiconductors,[18,19] insulators,[19,20] surfaces,[21] nanostructures,[22] and molecules.[23] This development is based on calculations that fully take quasiparticle (QP) electronic structures and excitonic as well as local-field effects (LFEs) into account (see Refs. 13 and 24 and references therein). Such many-body effects drastically influence the line shape, peak positions, and peak intensities, especially of the optical absorption spectra.

In the first step of the description, going from the independent-particle approximation to the independent-QP approximation,[25] the optically excited non-interacting electron-hole pairs are replaced by non-interacting quasielectron-quasihole pairs. In general, the optical absorption spectra are significantly blue-shifted;[14] the overall line shape is influenced because this shift is larger for peaks at higher energies.[26,27] For some of the peaks the spectral picture[28] based on critical points and van Hove singularities in the interband transitions between occupied QP valence bands (VBs) and empty QP conduction bands (CBs) remains valid.

In a second step, the screened attractive and unscreened repulsive interaction of quasielectrons and quasiholes is taken into account. This leads to a drastic redistribution of spectral strength from higher to lower photon energies combined with a redshift; this renders the picture of van Hove singularities questionable.[15] In addition, the absorption edge may be significantly modified by the formation of bound excitonic states,[29–31] a phenomenon which may also appear in resonance at higher optical transitions.[15,27]

Such sophisticated calculations have been previously carried out for group-III nitrides in the *wz* or the zinc-blende structure.[15,29,32–37] The resulting absorption coefficients and imaginary parts of the dielectric function (DF) are able to explain experimental findings: Independent of the crystal struc-

ture, energy positions as well as intensities of main peak structures are well described, even in the energy range of higher interband transitions. Even though the real and imaginary parts of the DFs of the nitrides[15,29,32–37] are much smaller than those of other semiconductors such as silicon,[14] well-converged calculations of optical spectra including QP and excitonic effects are possible nowadays. This is attributed, for instance, to a very dense **k**-point sampling as well as optical transition matrix elements derived from all-electron-like wave functions that allow for an accurate description of non-metals with small oscillator strengths.

In this paper, calculations of the electronic structure and the optical spectra of *wz*-$In_xGa_{1-x}N$ and *wz*-$In_xAl_{1-x}N$ alloys are presented and used to study the frequency-dependent DFs for different light polarizations and cluster statistics. In Sec. II the methodology is described and computational details are given. The success of the methods is demonstrated for the binary end components InN, GaN, and AlN in Sec. III. The influence of the alloy statistics and the composition on the main peaks of the DFs as well as the dielectric constants is studied in detail in Sec. IV. Finally, in Sec. V a brief summary and conclusions are presented.

II. THEORETICAL AND COMPUTATIONAL APPROACHES

A. Modeling of alloys

The $In_xX_{1-x}N$ (X=Ga, Al) alloy may consist of N cations and N anions. Within a cluster expansion[16,38–40] it is divided into M clusters, each of which consists of $2n$ atoms, n cations and n anions (nitrogen). Consequently, it holds $N = nM$ for the total number of atoms on each of the sublattices. Due to symmetry (before ionic relaxation) the clusters can be grouped into $J+1$ different classes. Each class $j = 0, \ldots, J$ comprises g_j clusters of the same total energy and contributes with the cluster fraction $x_j = M_j/M$ to the macroscopic alloy that is built by a set of $\{M_j\}$ clusters. The number of In atoms in each class is denoted by n_j. Since the x_j describe the statistical weights, they are normalized according to $\sum_{j=0}^{J} x_j = 1$ and $\sum_{j=0}^{J} n_j x_j = xn$ for an alloy of the average composition x.

As done in previous works on wurtzitic systems,[5,16,17,41] we use 16-atom clusters (i.e., $n = 8$) that consist of four *wz* unit cells. The possible total number of $\sum_{j=0}^{J} g_j = 2^n = 256$ clusters is divided into 22 classes and we use the atomic geometries that are described in Ref. 5. For thermodynamic-equilibrium conditions at a given temperature and composition, the x_j can be determined within the generalized quasi-chemical approximation (GQCA).[40,42]

Here, we study two limiting cases: (i) the strict-regular solution (SRS) model[42] for a random alloy (high-temperature limit of the GQCA) with cluster fractions

$$x_j^{\mathrm{SRS}}(x) = g_j x^{n_j} (1-x)^{n-n_j} \tag{1}$$

and (ii) the microscopic decomposition model (MDM)

$$x_j^{\mathrm{MDM}}(x) = \begin{cases} 1-x & \text{for} \quad j=0 \\ x & \text{for} \quad j=J \\ 0 & \text{otherwise} \end{cases}, \tag{2}$$

which describes the low-temperature limit of the GQCA with the strongest fluctuations of the composition on a microscopic length scale.[16,17]

The configurational average for a certain property of the alloy is related to the property P_j of a cluster material via the Connolly-Williams formula[40,43]

$$P(x) = \sum_{j=1}^{J} x_j(x) P_j. \tag{3}$$

The bowing of the composition dependence of an alloy property P can be described by[5]

$$P(x) = xP(\mathrm{InN}) + (1-x)P(\mathrm{XN}) - x(1-x)P_{\mathrm{b}}(x) \tag{4}$$

$$P_{\mathrm{b}}(x) = P_{\mathrm{b},0}/(1+P_{\mathrm{b},1}x^2) \tag{5}$$

with a bowing parameter $P_{\mathrm{b}}(x)$ that can be composition-dependent itself, as indicated by Eq. (5). In this work, we investigate the frequency-dependent DF $\varepsilon_{\perp/\parallel}(\omega)$ for perpendicular (ordinary) and parallel (extraordinary) light polarization (with respect to the c axis) as cluster properties. For each of the two alloys the spectra were computed for the 22 individual cluster classes.

B. Quasiparticle electronic structure

It is well known that the Kohn-Sham eigenvalues of density functional theory (DFT) cannot be identified with single-QP excitation energies $\varepsilon_{\nu\mathbf{k}}^{\mathrm{QP}}$ (band ν, Bloch wave vector $\mathbf{k}$).[44] Recently, we demonstrated for AlN, InN, and GaN that a QP calculation based on Hedin's *GW* approximation starting from eigenvalues and eigenfunctions obtained using the non-local hybrid HSE06 exchange-correlation (XC) functional[45] (see also Refs. 46 and 47) yields interband energies in excellent agreement with measured results.[5,15,48–50] This so-called HSE+G_0W_0 approach is, however, computationally too expensive for using it to calculate the starting electronic structure (QP eigenvalues, wave functions, Coulomb matrix elements) needed to set up the excitonic Hamiltonian. In addition, also the large number of **k** points required to converge the optical spectra (e.g. in the vicinity of the absorption edge or in the frequency region where the imaginary part of the DF is rather constant) for all 44 cluster cells makes it necessary to use a less expensive approach.

Therefore we pursue the procedure of Schleife *et al.*[27,51] where the HSE+G_0W_0 QP eigenvalues and wave functions are mimicked by those of a DFT+U approach and an additional scissors shift Δ.[13,17,30,37] The parameter U describes a potential acting on the Ga $3d$ and In $4d$ shell and is determined in such a way that the corresponding semicore binding energies resemble the HSE+G_0W_0 values. The scissors op-

erator Δ is used to open up the resulting band gaps to match the HSE+G_0W_0 ones. In order for this DFT+U+Δ scheme to work, the DFT+U gap has to be finite for all the cluster materials. When the AM05 XC functional is used,[5] this is, however, not the case for InN even for unrealistically large values of U. For that reason we employ the local density approximation (LDA), as parametrized by Perdew and Zunger,[52] to describe the XC functional. Two values for U, 5.7 eV (Ga 3d) and 3.7 eV (In 4d), are necessary for all clusters because of the different localization of the Ga and In d states. The LDA+U approach increases the LDA band gaps of the binary end components from 0.0 (wz-InN), 2.099 (wz-GaN), and 4.385 eV (wz-AlN) to 0.386, 2.474, and 4.385 eV, respectively.

Since these gaps are still smaller than HSE+G_0W_0 results (0.638, 3.571 and 6.328 eV for the binary end components) the scissors operator Δ is used to rigidly shift the CBs towards higher energy. The scissors shifts are derived for each cluster j so that the fundamental gaps are identical to the HSE+G_0W_0 results published before.[5] They vary non-linearly with n_j between 0.252 eV (InN), 1.097 eV (GaN), and 1.943 eV (AlN).

C. Frequency-dependent dielectric function

In order to describe optical properties of the alloys, their frequency-dependent macroscopic DF $\varepsilon_{\perp/\parallel}(\omega)$ is studied as central quantity. For nitrides it has been shown before that for their accurate description, the attractive electron-hole interaction has to be taken into account.[15,29,32–37] In addition, in order to obtain the macroscopic DF, LFEs are essential. Neglecting the dynamics of the screening, the inhomogeneous Bethe-Salpeter equation[13,14,24] for the optical polarization function[53,54] can be replaced by a homogeneous eigenvalue problem for the singlet electron-hole pair Hamiltonian[13,14,37]

$$\begin{aligned}\hat{H}(cv\mathbf{k},c'v'\mathbf{k}') = &\left[\varepsilon^{\mathrm{QP}}_{c\mathbf{k}}-\varepsilon^{\mathrm{QP}}_{v\mathbf{k}}\right]\delta_{cc'}\delta_{vv'}\delta_{\mathbf{k}\mathbf{k}'}\\ &-W(cv\mathbf{k},c'v'\mathbf{k}')+2\overline{v}(cv\mathbf{k},c'v'\mathbf{k}').\end{aligned} \tag{6}$$

The first summand in Eq. (6) describes the non-interacting quasielectron-quasihole pairs. The second term represents the screened Coulomb attraction W of pairs $cv\mathbf{k}$ and $c'v'\mathbf{k}'$, while the third contribution describes their electron-hole exchange interaction and, hence, the LFEs. The eigenvalues E_Λ and eigenvectors $A_\Lambda(cv\mathbf{k})$ of the pair Hamiltonian, Eq. (6), lead to the macroscopic DF via

$$\begin{aligned}\varepsilon_{\perp/\parallel}(\omega) =& 1+\frac{8\pi e^2\hbar^2}{Vm^2}\sum_\Lambda\left|\sum_{c,v,\mathbf{k}}\frac{\langle c\mathbf{k}\left|\mathbf{e}_{\perp/\parallel}\cdot\mathbf{p}\right|v\mathbf{k}\rangle}{\varepsilon_{c\mathbf{k}}-\varepsilon_{v\mathbf{k}}}A^*_\Lambda(cv\mathbf{k})\right|^2\times\\ &\times\sum_{\kappa=+,-}\frac{1}{E_\Lambda-\kappa\hbar(\omega+i\gamma)}\end{aligned} \tag{7}$$

with the momentum operator $\mathbf{p}$ and the ordinary/extraordinary light polarization vector $\mathbf{e}_{\perp/\parallel}$. V denotes the volume of the crystal and γ describes the inverse electron-hole pair lifetime (chosen to be $\gamma = 0.1$ eV).

A model for the DF[55,56] is used to describe the screening of the Coulomb potential in Eq. (6), which requires the static electronic dielectric constant ε_∞ for each cluster material. We employ the values calculated within random-phase approximation using the LDA+U scheme and averaged over the two independent components of the dielectric tensor. The number of conduction bands and $\mathbf{k}$-points guarantee a convergence of the dielectric constant on the order of 0.01 or better.

A converged description of the absorption onset requires a very dense $\mathbf{k}$-point sampling[15,30] of the low-energy optical transitions, much higher than it is necessary for calculations within the independent-QP approximation.[25] At the same time, describing the DF in a wide energy range renders the inclusion of a large number of CBs necessary. In order to fulfill both requirements, we employ different $\mathbf{k}$-point meshes for different photon energies: (i) A dense $9\times9\times9$ Monkhorst-Pack (MP)[57] $\mathbf{k}$-point mesh is used to describe pair energies up to 3.5 eV (6.3 eV) in InGaN (InAlN), i.e., in the vicinity of the absorption edge. (ii) Photon energies up to 10 eV are described using a $6\times6\times6$ MP mesh and, (iii) all higher excitations up to 20 eV are computed using a less dense $4\times4\times4$ MP $\mathbf{k}$-point mesh. Thereby, the number of bands (conduction bands) used for each $\mathrm{In}_{n_j}\mathrm{X}_{8-n_j}\mathrm{N}$ cluster material have been increased from 128 (96) in pure AlN to 288 (216) in pure InN according to the increasing number of d electrons in the cells. For InGaN 288 (216) bands (conduction bands) were used for all j.

This procedure still leads to large electron-hole pair Hamiltonians, Eq. (6), with ranks of up to 150,000; it is prohibitively expensive to directly diagonalize matrices that large. Instead, we compute the DFs for all the cluster materials using a time-propagation method[14] that relies only on matrix-vector multiplications and, hence, scales quadratically with the rank.

D. Computational framework

We use the Vienna Ab-Initio Simulation Package (VASP) to carry out the LDA+U calculations[58] that are necessary to set up[13,59] the excitonic Hamiltonians for each cluster material. The pseudopotentials have been generated within the projector-augmented-wave method[60,61] that allows us to compute valence s and p electronic states as well as In 4d and Ga 4d semicore states at all-electron quality. The wave functions are expanded into plane waves with a cutoff energy of 400 eV. Optical-transition matrix elements are computed within the longitudinal approximation.[62]

III. RESULTS FOR THE BINARY END COMPONENTS

A. Electronic structure

In order to illustrate the HSE+G_0W_0 QP results obtained in Ref. 50 for AlN, GaN, and InN in Fig. 1, we show the joint band structure together with the joint density of states (JDOS) for interband transitions $\varepsilon^{\mathrm{QP}}_{c\mathbf{k}}-\varepsilon^{\mathrm{QP}}_{v\mathbf{k}}$ from the uppermost six VBs ($v=v$) into the CBs ($v=c$). The direct fundamental

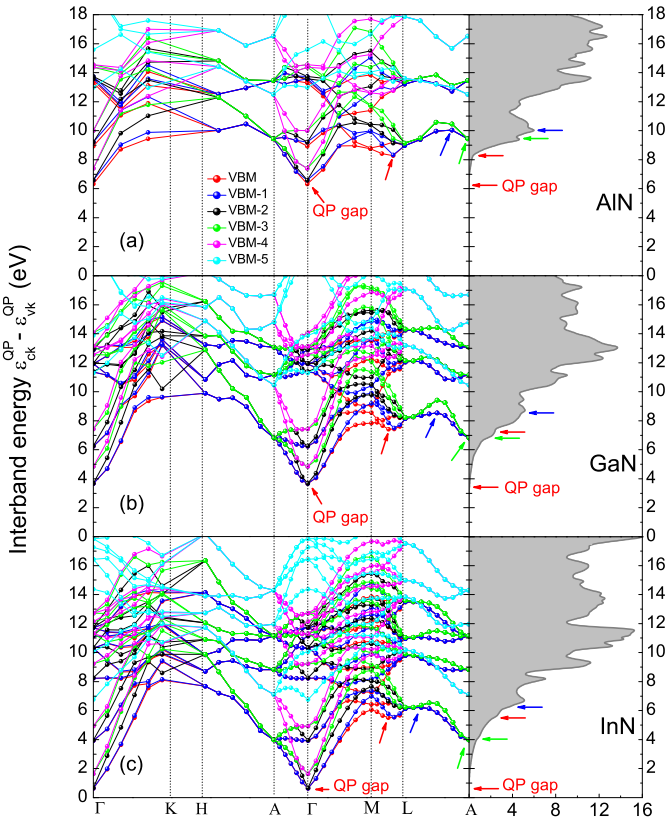

FIG. 1. (Color online) Joint QP band structure and joint density of states (in eV^{-1}) for (a) *wz*-AlN, (b) *wz*-GaN, and (c) *wz*-InN as calculated within the HSE+G_0W_0 approach. Arrows indicate the lowest-energy van Hove singularities.

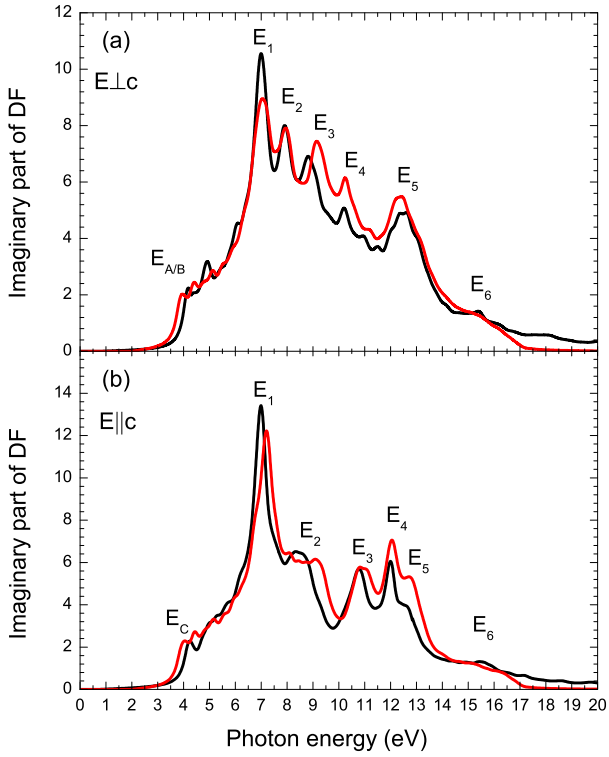

FIG. 2. (Color online) Imaginary part of (a) ordinary and (b) extraordinary DF of *wz*-GaN calculated for 4-atom cells (red solid lines) and 16-atom cells (black solid lines).

gaps at Γ amount to $E_g = 6.31$, 3.66, and 0.64 eV which is close to experimental values.[50] For the discussion below we want to note that the resulting interband-transition energies and JDOS obtained within the LDA+U+Δ scheme used in this work are very similar to those displayed in Fig. 1.

In this figure interband extrema related to van Hove singularities are clearly visible; besides the minima at Γ and A, such extrema also occur, for instance, between M and L. The lowest interband minima around Γ give rise to an M_0-type onset of the JDOS and the lowest interband maxima on the $L-A$ line, i.e., M_3 van Hove singularities, are the reason for a pronounced peak-like structure in the JDOS. Two other low-energy M_0 or M_3 critical points at A and the $L-A$ line, respectively, are also indicated. For a more detailed discussion of critical points in AlN the reader is referred to Ref. 15.

B. Dielectric functions

In Fig. 2 we compare the results for the DF of bulk *wz*-GaN computed using a 4-atom cell to the ones obtained for a 16-atom cell. In the case of the 4-atom cell we used 16×16×10 **k**-point meshes and 216 CBs and for the 16-atom supercells the parameters described in Sec. II C were used. Figure 2 shows that the overall agreement between the spectra is good and the peak positions and intensities are only slightly different. The reason for the small discrepancies are variations in the Brillouin zone (BZ) sampling and, hence, of the interband transitions. This does not only slightly modify the respective JDOS, but also the coupling of individual single-particle VB-CB transitions as described by the electron-hole pair amplitude $A_\Lambda(cv\mathbf{k})$ in Eq. (7) (see the discussion of the consequences in Ref. 15).

In Fig. 3, the imaginary parts of the DF of *wz*-AlN, *wz*-GaN, and *wz*-InN, calculated for ordinary and extraordinary light polarization using the 16-atom cells, are compared to spectra measured by means of spectroscopic ellipsometry.[63–68] In this work, the labels $E_1, \ldots, E_6$ are assigned to the peaks according to the energetical ordering of the peak structures. We use $E_{A/B}$ (E_C) to denote the peak that can be attributed to the lowest excitonic bound state that occurs for ordinary (extraordinary) light polarization. The corresponding transitions can be traced back to the uppermost VBs for the binary end components:[5,50,69] Since we neglect spin-orbit coupling in this work, the labels A and B refer to transitions from the twofold degenerate Γ_5 valence states into the CBs and C is used for transitions from the Γ_1-type VB into the CBs.[5,50,69]

Apart from small deviations the agreement between theoretical and experimental spectra with respect to the peak heights and positions is good (cf. Fig. 3). Particularly in the case of InN it is much better than reported for earlier calculations.[34] Consequently, as indicated by Fig. 3, the ma-

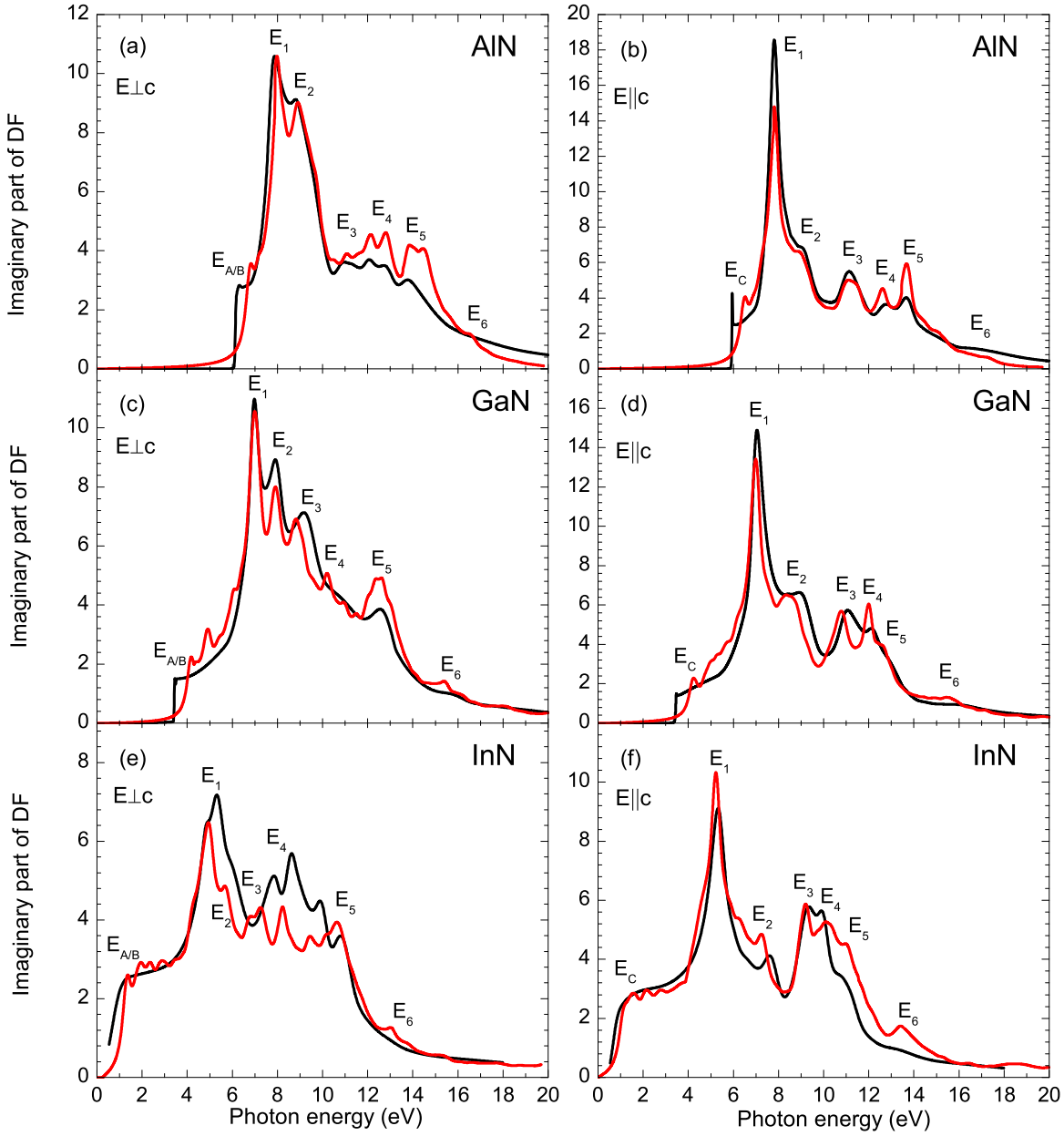

FIG. 3. (Color online) Imaginary part of the DF of *wz*-AlN (a, b), *wz*-GaN (c, d), and *wz*-InN (e, f) for ordinary (left panels) and extraordinary (right panels) light polarization. Red solid curves are calculated in this work using the 16-atom supercells. The spectra are compared to experimental results (black solid lines) for InN,[63,64] GaN,[65–67] and AlN.[65,66,68]

jority of the measured peaks can be easily identified with peaks in the theoretical spectrum. The agreement is particularly good for the most pronounced absorption peak E_1, especially for AlN and GaN. Small differences between theory and experiment are found for the positions of E_2 and E_3 for GaN and are attributed to using the same scissors shift for all interband transitions and, hence, neglecting the energy dependence of QP corrections. In addition, especially for InN, the theoretical spectra show wiggling structures above the absorption onset, whereas the experimental spectra show an almost plateau-like region of the DF; simulating such a behavior as a sum of broadened δ functions requires an even larger **k**-point density, which is computationally too difficult. The small deviations of the spectra of *wz*-AlN compared to those from another recent study[15] can be traced back to the use of slightly different atomic geometries resulting from the different approximations to XC.

Comparing the different spectra in Figs. 2 and 3 to the JDOS in Fig. 1 indicates the importance of excitonic/LFEs as well as of optical dipole matrix elements. The oscillator strengths in Eq. (7) are proportional to the inverse of the squared interband energies which leads to the ω^{-2} decrease

of the optical absorption for higher photon energies.[70]

IV. RESULTS FOR THE ALLOYS

A. Overall absorption spectra

For ordinary and extraordinary light polarization the configurational averages of the DFs of $In_xGa_{1-x}N$ and $In_xAl_{1-x}N$ have been computed according to Eqs. (3) and (7) using the SRS and the MDM alloy statistics. Their imaginary parts describe the optical absorption and are plotted in Figs. 4 and 5 for $0 \leq x \leq 1$ over a wide range of photon energies. These figures allow to follow the evolution of pronounced peak structures with the In composition x in the alloy. In the following, we discuss the influence of the alloy statistics on this behavior.

In the case of the MDM [cf. Eq. (2)], the spectra in Figs. 4(c), 4(d), 5(c), and 5(d) are clearly related to the spectra of the binary end components: the peak positions remain fixed at the values found for the binary systems (cf. Figs. 2 and 3) and the intensities are weighted by the probabilities $1-x$ (GaN or AlN) and x (InN). Also the energy position of the absorption onset remains unchanged over a large composition range. These findings contradict the results of room-temperature spectroscopic-ellipsometry measurements[7–10,66] that show a pronounced variation of the optical gaps as well as of interband critical points with x. Therefore, we now focus on the results obtained within the SRS statistics, which is also supported by the detailed studies of the fundamental gaps of nitride alloys elsewhere.[5]

The random distribution of the clusters corresponding to the SRS model [cf. Eq. (1)] leads to variations of the peak positions and heights that are nonlinear with x. Figures 4(a), 4(b), 5(a), and 5(b) suggest that it is possible to follow a certain peak over a wide range of compositions with a rather continuous variation of the line shapes. However, this observation is misleading since different clusters and, hence, different optical transitions contribute to such an individual peak structure as the composition x changes. Not only the intermixing of interband transitions by excitonic effects (that already occurs for the binary end components[15]) but also the alloying renders such an analysis impossible: even though a band structure and a BZ exists for each cluster material within the cluster expansion scheme, a symmetry analysis is not feasible due to the atomic relaxation of each cluster (which represents structural disorder) and the configurational average (which accounts for chemical disorder). For that reason it is not clear that electronic states of nearly the same symmetry contribute to a certain peak as the position and weight vary. We come back to this point in the next section.

Across the entire range of photon energies, the increasing influence of GaN [Figs. 4(a) and (b)] or AlN [Figs. 5(a) and (b)] becomes clear as x decreases from 1 to 0. The composition dependence is more pronounced for $In_xAl_{1-x}N$ than for $In_xGa_{1-x}N$, due to the larger fundamental band gap of AlN and the bigger range of weakly varying absorption between the onset and the first main peak in GaN. The variation of the main peak near 7.0 eV (GaN) or 7.5 eV (AlN) is weak and we will discuss the details of the higher interband transitions below.

While the influence of the different polarization directions is more striking near the end components, it is less pronounced for intermediate compositions x, as can be seen when comparing subfigures (a) and (b) of Figs. 4 and 5. One reason is that the structural disorder in the alloy modifies the dipole selection rules of higher-energy transitions. Hence, for compositions near the end components the *wz* symmetry is preserved better, leading to different dipole selection rules for both light polarizations.[50] In addition, fewer clusters contribute for compositions close to the binary end components.

B. Interband critical points

The occurrence of pronounced peak structures in the imaginary parts of the DFs shown in Figs. 4 and 5 suggests an analysis of the composition dependence of the peak positions similar to that done when interpreting experimental spectra.[7–10,66,71] The picture behind such an analysis relies on the decomposition of Eq. (7) into a sum of oscillators j with given energy E_j, oscillator strength C_j, and damping parameter Γ_j. Historically, this approach is driven by the idea that interband transitions govern the DF and due to the characteristic behavior of the JDOS in the vicinity of critical points (cf. Fig. 1) so-called van-Hove singularities occur.[28] According to the nature of the critical points such a picture can be refined by taking excitonic effects into account.[72] In the following we adopt this picture of van-Hove singularities despite its validity is limited due to the influence of optical transition matrix elements, excitonic effects, and contributions from $\mathbf{k}$ points other than the high-symmetry ones.[15]

The composition dependence of several characteristic energies $E_{A/B}$, E_C, and $E_1, \ldots, E_6$ has been derived from measured spectra based on this or a similar analysis.[7–10,71] For our analysis we relate the peaks $E_1, \ldots, E_6$ in the imaginary parts of the DFs of the binary end components to interband transitions at the Γ, M, K, A, L, and H high-symmetry points of the hexagonal BZ. Table I shows the energies of the corresponding transitions as derived within the LDA+U+Δ approach and their assignment to the different peaks is given. When comparing these transition energies to the peak positions in Figs. 4 and 5 one has to keep in mind that the interband energies are slightly higher than the peak energies because of the excitonic redshift. The results in Table I show that the identification of the peaks is possible, to some approximation, for the binary end components.

However, in addition to these difficulties of unequivocally relating interband energies to a specific peak position (see above), the composition dependence introduces a certain ambiguity for the alloys, because for intermediate compositions the translational and point-group symmetries of the end components are not present anymore. We find that the assignment of peaks for compositions close to the end components is easier for $In_xGa_{1-x}N$ than it is for $In_xAl_{1-x}N$ because $In_xAl_{1-x}N$ shows stronger internal strains and, hence, stronger atomic relaxations. Nevertheless, for instance the E_1 peak can be

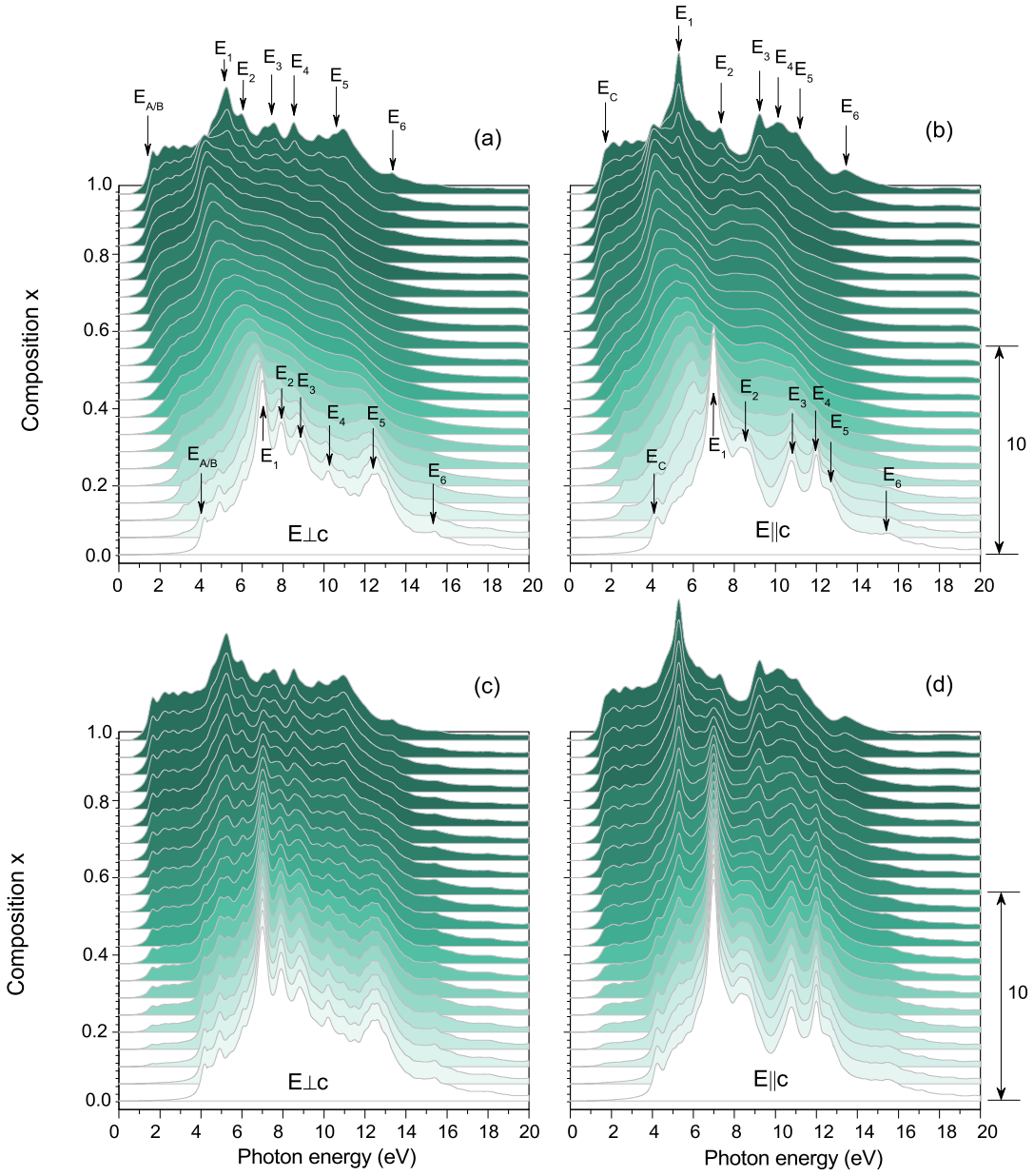

FIG. 4. (Color online) Imaginary part of the DF of *wz*-$In_xGa_{1-x}N$ for ordinary (a, c) and extraordinary (b, d) light polarization as a function of the In composition x. The results for two different alloy statistics, SRS (a, b) and MDM (c, d) model, are shown. The peaks $E_1, \ldots, E_6$ (see text) and the absorption onsets ($E_{A/B}$ and E_C) are labeled. The bar indicates the scale for $\mathrm{Im}\,\varepsilon_{\perp/\parallel}(\omega)$.

identified in the case of ordinary light polarization also for intermediate compositions x, where many classes of clusters contribute to the spectra. Its position changes from 8.1 eV (7.2 eV) at $x = 0$ to about 5.2 eV at $x = 1$ in $In_xAl_{1-x}N$ ($In_xGa_{1-x}N$). According to Table I and Fig. 1 the main contributions are related to the lowest interband transitions on the $L-M$ line in the BZ. While the identification seems to be obvious, for small x a second peak occurs for both $In_xAl_{1-x}N$ and $In_xGa_{1-x}N$ which can be described by a strong non-linear composition-dependent bowing parameter.

For each of the individual $In_{n_j}Ga_{8-n_j}N$ and $In_{n_j}Al_{8-n_j}N$ cluster materials we extracted the positions of the six peaks discussed above. The results for all clusters are given in Fig. 6 along with the corresponding configurational averages within the SRS alloy statistics. For the reasons described above, the peaks cannot always be unequivocally assigned, but for $In_xAl_{1-x}N$, the peak identification for clusters with intermediate composition is particularly difficult. Hence, dotted lines are plotted in order to indicate the uncertainties, and in the following we focus on $In_xGa_{1-x}N$ instead.

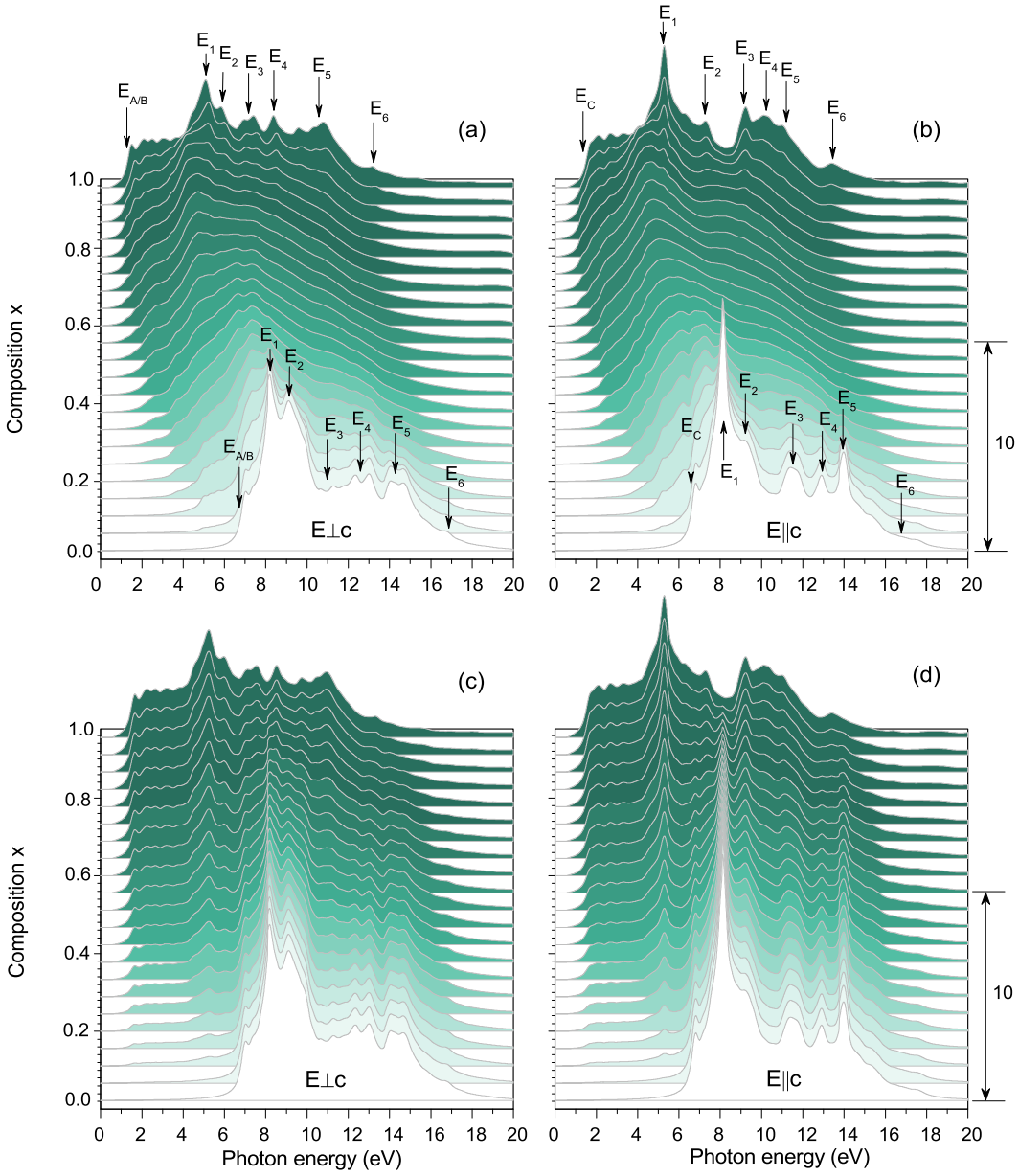

FIG. 5. (Color online) Imaginary part of the DF of *wz*-$In_xAl_{1-x}N$ for ordinary (a, c) and extraordinary (b, d) light polarization as a function of the In composition x. The results for two different alloy statistics, SRS (a, b) and MDM (c, d) model, are shown. The peaks $E_1, \ldots, E_6$ (see text) and the absorption onsets ($E_{A/B}$ and E_C) are labeled. The bar indicates the scale for $\mathrm{Im}\,\varepsilon_{\perp/\parallel}(\omega)$.

In general, the composition dependence of the peak maxima that is depicted in Fig. 6 exhibits a significant bowing which we describe by Eqs. (4) and (5). For the higher interband transitions in $In_xGa_{1-x}N$ this leads to the parameters given in Table II. These values (except for the ones for E_5) indicate that the bowing as described by $E_{b,0}$ is very similar or only slightly larger than the one obtained for the fundamental gaps.[5] The composition dependence of the bowing, quantified by $E_{b,1}$, is small. Only for the lowest absorption peaks $E_{A/B}$ and E_C larger values are predicted (cf. Table II).

The order of magnitude of the bowing parameters agrees with results derived from measured spectra[8,9] but the theoretical values tend to be slightly larger (see e.g. the bowing parameters b_i derived for $E_1, \ldots, E_6$ from measured data[8,9] and the ones given for $In_xGa_{1-x}N$ in Table I). The apparent overestimation of the bowing parameters by our calculations may be attributed to using only the limiting case of the SRS cluster statistics to derive the data in Table II. A cluster statistics that is closer to the MDM limit would lead to a significant reduction of the bowing. At the same time such an explanation is

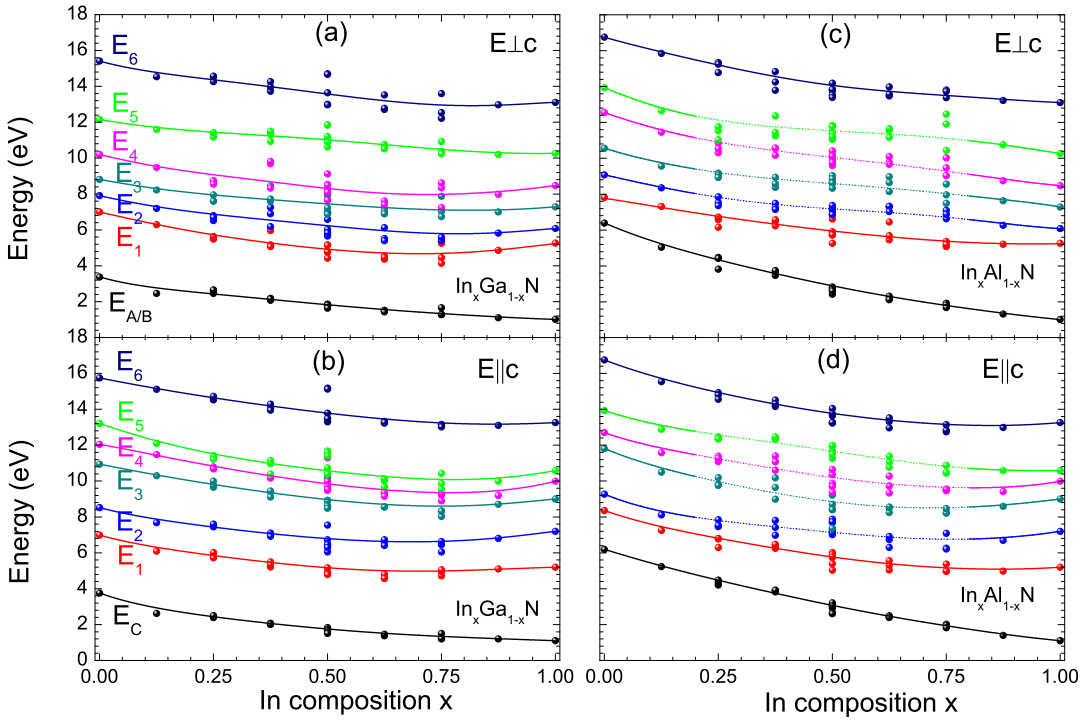

FIG. 6. (Color online) Configurational averages for the interband transition energies computed within the SRS model (solid lines) are shown for $In_xGa_{1-x}N$ (a, b) and $In_xAl_{1-x}N$ (c, d). Results for ordinary (a, c) and extraordinary (b, d) light polarization are given. Large dots represent the corresponding energies for individual clusters. The dotted lines in (c, d) indicate the difficulties to identify the symmetry of interband transitions especially for $In_xAl_{1-x}N$.

TABLE I. Characteristic interband energies (in eV) related to the peak positions $E_1, \ldots, E_6$ in Figs. 4 and 5 for ordinary and extraordinary light polarization. The symmetry character and the position of the VB and CB extrema that determine the interband energy in the BZ are indicated. The interband energies follow from the LDA+U+Δ approach and slightly differ from the HSE+G_0W_0 results in Fig. 1.

Peak	Transition	Polarization	AlN	GaN	InN
E_1	$U_4 - U_1$	$\perp, \parallel$	–	6.57	4.63
	$M_4 - M_1$	$\perp, \parallel$	8.36	6.90	5.26
	$L_{1,3} - L_{1,3}$	$\parallel$	8.58	7.26	5.27
E_2	$M_2 - M_1$	$\perp$	9.80	8.12	6.08
	$K_3 - K_2$	$\parallel$	9.27	8.49	6.92
E_3	$H_3 - H_{1,2}$	$\parallel$	10.56	9.38	7.29
	$K_3 - K_3$	$\perp$	–	10.97	8.81
	$K_3 - K_2$	$\perp$	11.81	10.94	8.64
	$L_{1,3} - L_{1,3}$	$\perp$	–	10.59	9.10
E_4	$L_{1,3} - L_{1,3}$	$\perp$	12.55	10.57	8.43
	$L_{1,3} - L_{1,3}$	$\perp, \parallel$	12.93	10.59	9.10
	$L_{2,4} - L_{1,3}$	$\perp$	12.66	10.58	8.48
	$A_{5,6} - A_{1,6}$	$\parallel$	–	12.16	9.74
E_5	$A_{5,6} - A_{1,6}$	$\parallel$	–	12.16	10.27
	$H_3 - H_3$	$\parallel$	14.23	12.15	–
	$A_{1,3} - A_{5,6}$	$\parallel$	–	13.51	10.87
E_6	$A_{1,3} - A_{1,6}$	$\perp, \parallel$	16.75	15.41	13.11

TABLE II. Coefficients of the bowing parameter for higher interband transitions in the optical absorption spectra of Fig. 4 for $In_xGa_{1-x}N$. Values for ordinary and extraordinary light polarizations are given.

Transition	ordinary		extraordinary	
	$E_{b,0}$	$E_{b,1}$	$E_{b,0}$	$E_{b,1}$
1	4.43	−0.25	3.81	0.17
2	2.85	−0.44	3.98	−0.25
3	2.35	−0.34	3.51	−0.42
4	3.67	−0.43	3.83	−0.63
5	0.90	−0.54	5.16	−0.25
6	2.45	0.57	2.54	−0.43
A/B, C	2.07	1.16	3.82	1.47

somewhat in contrast to the findings for the fundamental absorption edge discussed in a previous paper,[5] where we have clearly stated that the composition dependence of the fundamental gap and the corresponding bowing (measured by absorption instead of photoluminescence) can be approximately explained using the SRS model. In this paper it is also clearly illustrated that fluctuations of observable quantities influence the bowing at a given average composition.

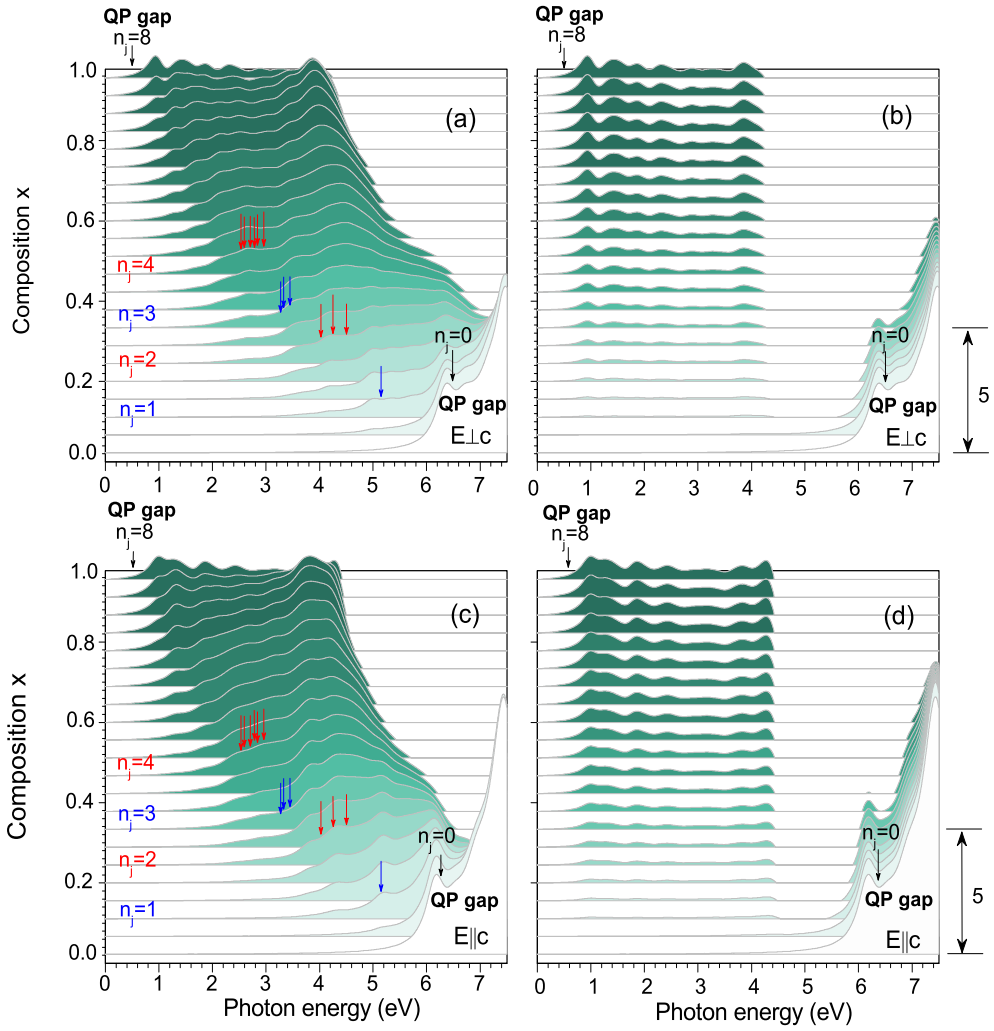

FIG. 7. (Color online) Difference of the imaginary parts of the DFs with and without excitonic/LFEs for $In_xAl_{1-x}N$. Results are shown for ordinary (a, b) and extraordinary (c, d) light polarization as well as the MDM (b, d) and the SRS model (a, c). The arrows indicate the QP gaps of the clusters that significantly contribute to the spectrum for a given average composition x. Only positive differences are shown (see text). The bar indicates the scale for the z axis.

C. Excitonic effects

Because of the small dielectric constant of AlN (see Sec. IV D), the excitonic effects are expected to be strongest for $In_xAl_{1-x}N$ alloys with small compositions x. This is confirmed by the values of the binding energies of the band-edge excitons that are largest (58 meV) for AlN[73] and smaller for GaN (26 meV)[74] and InN (4 meV).[30] Hence, we focus on $In_xAl_{1-x}N$ for the illustration of the excitonic effects in Fig. 7, where we plot the difference of the imaginary parts of the DFs with and without excitonic and LFEs. In Fig. 7 we distinguish between the two polarization directions as well as the MDM and the SRS model. We show only positive values of the difference for the spectral regions around the absorption edges of the individual cluster materials to illustrate the most important excitonic effects due to bound exciton states, Coulomb enhancement of the absorption edge, and redistribution of spectral strength from higher to lower photon energies.

Due to the large screening in InN and GaN-rich alloys, bound-state-related peaks are only visible for AlN-rich alloys in Fig. 7. This becomes particularly clear from the difference spectra obtained within the MDM [cf. Figs. 7(b) and (d)] as they represent a linear interpolation of the difference spectra for the binary end components: For InN-rich alloys a redistribution of spectral strength as well as a Coulomb enhancement[28] is found, however, a peak related to excitonic bound states (due to transitions from the Γ_5- or Γ_1-type VB maximum) is only visible at the absorption onset of AlN-rich alloys. In the case of the SRS model, the difference spectra [see Figs. 7(a) and (c)] are completely different for intermediate compositions x. As discussed before, there is a continuous variation of the absorption edge modified by excitonic effects

for compositions varying from $x = 0$ to $x = 1$.

In addition, in Fig. 7, small arrows mark the QP gaps of individual clusters that significantly contribute to the configurational average of the spectrum corresponding to a certain composition x. This is important for the SRS model because peaks that correspond to bound excitons of individual clusters may occur in the configurational average for the DF. In principle, these peaks represent resonant states in the DF since they appear near the energy position of the QP gap of the respective cluster, i.e., below the arrows in Figs. 7(a) and (c). In the alloy, clusters with a different composition already absorb light at these photon energies. Indeed such a "bound" excitonic state below the QP edge occurs for the $In_1Al_7N_8$ cluster material ($n_j = 1$) for both polarization directions and also for $n_j = 2$ such peaks are found. While their energy position does not significantly depend on the average composition x of the random alloy, the intensities are drastically reduced with increasing composition.

Since we calculate the spectrum of each individual cluster material using a periodic structure based on a 16-atom supercell, local confinement effects on the electrons or holes are not taken into account. Quantum confinement related to strong composition fluctuations on a length scale of a few nm is not included in the present alloy description. The excitonic features computed within this work belong to a class of Wannier-Mott-like excitons.[28] Only those Wannier-Mott excitons with Bohr radii smaller than the extent of characteristic composition fluctuations Δx are correctly described within our approach to compute the configurational average. Using an effective-mass approximation[28] for the exciton binding, we estimate that the Bohr radii may vary in a range between about 1 nm (AlN-rich) and 10 nm (In-rich). When clustering and/or composition fluctuations[5,34] occur on a length scale that is smaller than those numbers for the Bohr radii, our approach cannot correctly describe the excitonic effects.

D. Dielectric properties

The real part of the DF at vanishing frequency, Re $\varepsilon(\omega = 0) \equiv \varepsilon_\infty$, describes the tensor of the macroscopic electronic dielectric constant. In hexagonal crystals, it has two independent components $\varepsilon_{\infty,\perp}$ and $\varepsilon_{\infty,\parallel}$. In contrast to many other theoretical works, we computed macroscopic electronic dielectric constants including excitonic and local-field effects and not only values within the independent-particle or independent-QP approximation.[25] We observe that the values for the macroscopic dielectric constants $\varepsilon_{\infty,\perp}$ and $\varepsilon_{\infty,\parallel}$ within independent-particle approximation are by about $0.3 \ldots 0.8$ smaller.

Using our approach, we obtain $\varepsilon_{\infty,\perp} = 4.12$, 5.11, and 7.86 as well as $\varepsilon_{\infty,\parallel} = 4.32$, 5.30, and 8.74 for AlN, GaN, and InN, respectively. The corresponding experimental values,[75,76] $\varepsilon_{\infty,\perp} = 4.14$, 5.19, and 7.83 as well as $\varepsilon_{\infty,\parallel} = 4.28$, 5.32, and 8.03, are in excellent agreement. In the case of *wz*-InN (extraordinary light polarization) the theoretical result slightly overestimates (by about 0.7) the electronic dielectric constant. This can be a consequence of our numerical approach, i.e. the used LDA+U+Δ method; the wave functions and, hence, the oscillator strengths might have a particularly large impact in the case of InN, which has the smallest energy gap. Also experimental problems due to the difficulties to precisely measure the dielectric constant for light polarization parallel to the c-axis in real samples cannot be excluded. Moreover, sample quality problems related to the real structure such as strain, free carriers, surfaces and interfaces may occur.

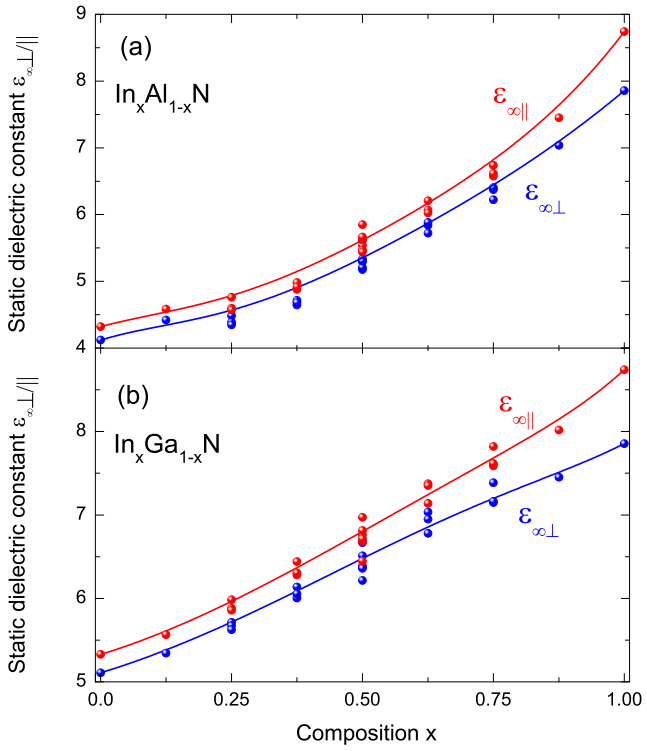

FIG. 8. (Color online) The independent components $\varepsilon_{\infty,\perp}$ (blue, ordinary polarization) and $\varepsilon_{\infty,\parallel}$ (red, extraordinary polarization) are plotted versus the average composition x for (a) $In_xAl_{1-x}N$ and (b) $In_xGa_{1-x}N$ alloys described within the SRS model. The values for the individual cluster materials are indicated by dots.

The results for the configurational averages within the SRS model are plotted in Fig. 8 using the dielectric constants (including excitonic and local-field effects) calculated in this work. In order to illustrate the influence of the local geometries, also the dielectric constants for the individual cluster materials are depicted in this figure. Figure 8 indicates some bowing, similar to the one found for the fundamental energy gaps.[5] We describe the variation of the dielectric constants with the composition using Eq. (4) along with a composition-independent bowing parameter $\Delta\varepsilon_{\infty,\perp/\parallel}$. The bowing is most pronounced for the $In_xAl_{1-x}N$ alloy, where $\Delta\varepsilon_{\infty,\perp} = 2.54$ and $\Delta\varepsilon_{\infty,\parallel} = 3.77$. For $In_xGa_{1-x}N$ we obtain $\Delta\varepsilon_{\infty,\perp} = 0.09$ and $\Delta\varepsilon_{\infty,\parallel} = 1.05$. The calculated composition dependence of $\varepsilon_{\infty,\perp}(x)$ for the AlN-rich alloy is close to variations found in experiment.[10]

V. SUMMARY AND CONCLUSIONS

The optical properties of *wz*-$In_xGa_{1-x}N$ and *wz*-$In_xAl_{1-x}N$ alloys have been described using two basic approximations: (i) The alloys are modeled based on a cluster expansion method where each alloy is divided into clusters of 22 artificial materials. The cluster statistics is described by two limiting cases: a strict regular solution and a decomposition on a microscopic length scale. The corresponding probabilities to find a certain cluster material in the alloy have been employed to perform the configurational averages for the frequency-dependent DFs using the DFs calculated for the individual cluster materials. (ii) In order to derive these individual DFs we have applied sophisticated many-body approaches. Extremely dense **k**-point meshes were used and the QP electronic structure was approximated within the LDA+U+Δ scheme. The screened Coulomb attraction of quasielectrons and quasiholes as well as the unscreened electron-hole exchange interaction are taken into account.

By comparing the composition dependence of the resulting absorption spectra to experimental findings for a wide photon-energy range, we find indications that the cation distribution in the chemically disordered ternary compounds is better described by the strict regular solution model. At least, the variation of higher-energy absorption peaks described within the SRS approach seems to fit better to experimental findings.

Close to the binary end components, important spectral features can approximately be explained by critical points in the band structure. However, for intermediate average compositions x such a relation between electronic structure and optical absorption peaks becomes impossible, especially for $In_xAl_{1-x}N$. The bowing of higher interband transition energies versus composition is smaller than that found for the absorption edge. Excitonic and LFEs influence the entire spectra. However, despite alloying bound excitons remain visible below the absorption edge, especially for AlN-rich alloys.

The macroscopic dielectric constants calculated for the binary end components agree well with recent experimental findings. They show a significant bowing for intermediate compositions in $In_xAl_{1-x}N$ while the bowing is much smaller for $In_xGa_{1-x}N$.

ACKNOWLEDGMENTS

We thank C. Rödl for interesting scientific discussions. The research presented here has received funding from the European Community's Seventh Framework Programme within the EU ITN RAINBOW (Grant No. 2008-2133278). Part of this work was performed under the auspices of the U.S. Department of Energy at Lawrence Livermore National Laboratory under Contract DE-AC52-07A27344.

* luiz-claudio.de-carvalho@uni-jena.de

1 J. Wu, Journal of Applied Physics **106**, 011101 (2009).
2 V. Davydov, A. Klochikhin, R. Seisyan, V. Emtsev, S. Ivanov, F. Bechstedt, J. Furthmüller, H. Harima, A. Mudryi, A. Aderhold, O. Semchinova, and J. Graul, Physica Status Solidi B **229**, R1 (2002).
3 J. Wu, W. Walukiewicz, K. M. Yu, J. W. Ager III, E. E. Haller, H. Lu, W. J. Schaff, Y. Saito, and Y. Nanishi, Appl. Phys. Lett. **80**, 3967 (2002).
4 I. Vurgaftman and J. R. Meyer, Journal of Applied Physics **94**, 3675 (2003).
5 L. C. de Carvalho, A. Schleife, J. Furthmüller, and F. Bechstedt, Phys. Rev. B **85**, 115121 (2012).
6 P. Schley, R. Goldhahn, A. T. Winzer, G. Gobsch, V. Cimalla, O. Ambacher, M. Rakel, C. Cobet, N. Esser, H. Lu, and W. J. Schaff, Phys. Status Solidi B **243**, 1572 (2006).
7 P. Schley, R. Goldhahn, A. T. Winzer, G. Gobsch, V. Cimalla, O. Ambacher, H. Lu, M. Schaff, W. J.and Kurouchi, Y. Nanishi, M. Rakel, and N. Cobet, C.and Esser, Phys. Rev. B **75**, 205204 (2007).
8 E. Sakalauskas, H. Behmenburg, P. Schley, G. Gobsch, C. Giesen, H. Kalisch, R. H. Jansen, M. Heuken, and R. Goldhahn, Phys. Status Solidi A **208**, 1517 (2011).
9 R. Goldhahn, P. Schley, A. T. Winzer, G. Gobsch, V. Cimalla, O. Ambacher, M. Rakel, C. Cobet, N. Esser, H. Lu, and W. J. Schaff, Phys. Status Solidi A **203**, 42 (2006).
10 E. Sakalauskas, H. Behmenburg, C. Hums, P. Schley, G. Rossbach, C. Giesen, M. Heuken, H. Kalisch, R. H. Jansen, J. Bläsing, A. Dadgar, A. Krost, and R. Goldhahn, J. Phys. D Appl. Phys. **43**, 365102 (2010).
11 C. Buchheim, R. Goldhahn, M. Rakel, C. Cobet, N. Esser, U. Rossow, D. Fuhrmann, and A. Hangleiter, Phys. Status Solidi B **242**, 2610 (2005).
12 I. Gorczyca, S. P. Łepkowski, T. Suski, N. E. Christensen, and A. Svane, Phys. Rev. B **80**, 075202 (2009).
13 C. Rödl, F. Fuchs, J. Furthmüller, and F. Bechstedt, Phys. Rev. B **77**, 184408 (2008).
14 W. G. Schmidt, S. Glutsch, P. H. Hahn, and F. Bechstedt, Phys. Rev. B **67**, 085307 (2003).
15 A. Riefer, F. Fuchs, C. Rödl, A. Schleife, F. Bechstedt, and R. Goldhahn, Phys. Rev. B **84**, 075218 (2011).
16 A. Schleife, M. Eisenacher, C. Rödl, F. Fuchs, J. Furthmüller, and F. Bechstedt, Phys. Rev. B **81**, 245210 (2010).
17 A. Schleife, C. Rödl, J. Furthmüller, and F. Bechstedt, New J. Phys. **13**, 085012 (2011).
18 S. Albrecht, L. Reining, R. Del Sole, and G. Onida, Phys. Rev. Lett. **80**, 4510 (1998).
19 L. X. Benedict, E. L. Shirley, and R. B. Bohn, Phys. Rev. Lett. **80**, 4514 (1998).
20 M. Rohlfing and S. G. Louie, Phys. Rev. Lett. **81**, 2312 (1998).
21 P. H. Hahn, W. G. Schmidt, and F. Bechstedt, Phys. Rev. Lett. **88**, 016402 (2001).
22 M. Bruno, M. Palummo, A. Marini, R. D. Sole, and S. Ossicini, Phys. Rev. Lett. **98**, 036807 (2007).
23 P. H. Hahn, W. G. Schmidt, and F. Bechstedt, Phys. Rev. B **72**, 245425 (2005).
24 M. Rohlfing and S. G. Louie, Phys. Rev. B **62**, 4927 (2000).
25 B. Adolph, V. I. Gavrilenko, K. Tenelsen, F. Bechstedt, and R. Del Sole, Phys. Rev. B **53**, 9797 (1996).
26 A. Schleife, *Electronic and optical properties of MgO, ZnO, and*

CdO (Südwestdeutscher Verlag für Hochschulschriften, 2011).
[27] A. Schleife, C. Rödl, F. Fuchs, J. Furthmüller, and F. Bechstedt, Phys. Rev. B **80**, 035112 (2009).
[28] P. Yu and M. Cardona, *Fundamentals of Semiconductors* (Springer-Verlag, Berlin, 1999).
[29] R. Laskowski, N. E. Christensen, G. Santi, and C. Ambrosch-Draxl, Phys. Rev. B **72**, 035204 (2005).
[30] F. Fuchs, C. Rödl, A. Schleife, and F. Bechstedt, Phys. Rev. B **78**, 085103 (2008).
[31] A. Schleife, C. Rödl, F. Fuchs, K. Hannewald, and F. Bechstedt, Phys. Rev. Lett. **107**, 236405 (2011).
[32] L. X. Benedict and E. L. Shirley, Phys. Rev. B **59**, 5441 (1999).
[33] L. Benedict, T. Wethkamp, K. Wilmers, C. Cobet, N. Esser, E. Shirley, W. Richter, and M. Cardona, Solid State Commun. **112**, 129 (1999).
[34] J. Furthmüller, P. H. Hahn, F. Fuchs, and F. Bechstedt, Phys. Rev. B **72**, 205106 (2005).
[35] F. Bechstedt, K. Seino, P. H. Hahn, and W. G. Schmidt, Phys. Rev. B **72**, 245114 (2005).
[36] P. H. Hahn, K. Seino, W. G. Schmidt, J. Furthmüller, and F. Bechstedt, Phys. Status Solidi B **242**, 2720 (2005).
[37] F. Bechstedt, F. Fuchs, and J. Furthmüller, Phys. Status Solidi A **207**, 1041 (2010).
[38] A. Sher, M. van Schilfgaarde, A.-B. Chen, and W. Chen, Phys. Rev. B **36**, 4279 (1987).
[39] S.-H. Wei, L. G. Ferreira, and A. Zunger, Phys. Rev. B **41**, 8240 (1990).
[40] L. K. Teles, J. Furthmüller, L. M. R. Scolfaro, J. R. Leite, and F. Bechstedt, Phys. Rev. B **62**, 2475 (2000).
[41] C. Caetano, L. K. Teles, M. Marques, A. Dal Pino, and L. G. Ferreira, Phys. Rev. B **74**, 045215 (2006).
[42] A.-B. Chen and A. Sher, *Semiconductor Alloys* (Plenum, New York, 1995).
[43] J. W. D. Connolly and A. R. Williams, Phys. Rev. B **27**, 5169 (1983).
[44] G. Onida, L. Reining, and A. Rubio, Rev. Mod. Phys. **74**, 601 (2002).
[45] J. Heyd, G. E. Scuseria, and M. Ernzerhof, J. Chem. Phys. **124**, 219906 (2006).
[46] J. Paier, M. Marsman, K. Hummer, G. Kresse, I. C. Gerber, and J. G. Ángyán, J. Chem. Phys. **124**, 154709 (2006).
[47] J. Paier, M. Marsman, K. Hummer, G. Kresse, I. C. Gerber, and J. G. Ángyán, J. Chem. Phys. **125**, 249901 (2006).
[48] F. Fuchs, J. Furthmüller, F. Bechstedt, M. Shishkin, and G. Kresse, Phys. Rev. B **76**, 115109 (2007).
[49] F. Bechstedt, F. Fuchs, and G. Kresse, Phys. Status Solidi B **246**, 1877 (2009).
[50] L. C. de Carvalho, A. Schleife, and F. Bechstedt, Phys. Rev. B **84**, 195105 (2011).
[51] A. Schleife, C. Rödl, F. Fuchs, J. Furthmüller, F. Bechstedt, P. H. Jefferson, T. D. Veal, C. F. McConville, L. F. J. Piper, A. DeMasi, K. E. Smith, H. Lösch, R. Goldhahn, C. Cobet, J. Zúñiga-Pérez, and V. Muñoz-Sanjosé, J. Korean Phys. Soc. **53**, 2811 (2008).
[52] J. P. Perdew and A. Zunger, Phys. Rev. B **23**, 5048 (1981).
[53] W. Hanke and L. J. Sham, Phys. Rev. Lett. **43**, 387 (1979).
[54] G. Strinati, Riv. Nuovo Cimento **11**, 1 (1988).
[55] F. Bechstedt, R. Del Sole, G. Cappellini, and L. Reining, Solid State Commun. **84**, 765 (1992).
[56] G. Cappellini, R. Del Sole, L. Reining, and F. Bechstedt, Phys. Rev. B **47**, 9892 (1993).
[57] H. J. Monkhorst and J. D. Pack, Phys. Rev. B **13**, 5188 (1976).
[58] G. Kresse and J. Furthmüller, Phys. Rev. B **54**, 11169 (1996).
[59] C. Rödl, F. Fuchs, J. Furthmüller, and F. Bechstedt, Phys. Rev. B **79**, 235114 (2009).
[60] P. E. Blöchl, Phys. Rev. B **50**, 17953 (1994).
[61] G. Kresse and D. Joubert, Phys. Rev. B **59**, 1758 (1999).
[62] M. Gajdoš, K. Hummer, G. Kresse, J. Furthmüller, and F. Bechstedt, Phys. Rev. B **73**, 045112 (2006).
[63] P. Schley, J. Räthel, E. Sakalauskas, G. Gobsch, M. Wieneke, J. Bläsing, A. Krost, G. Koblemüller, J. S. Speck, and R. Goldhahn, Phys. Status Solidi A **207**, 1062 (2010).
[64] R. Goldhahn, A. Winzer, V. Cimalla, O. Ambacher, C. Cobet, W. Richter, N. Esser, J. Furthmüller, F. Bechstedt, H. Lu, and W. J. Schaff, Superlattice Microst. **36**, 591 (2004).
[65] M. Röppischer, *Optische Eigenschaften von Aluminum-Galliumnitride-Halbleitern*, Ph.D. thesis, TU-Berlin (2011).
[66] M. Feneberg, M. Röppischer, C. Cobet, N. Esser, N. B., K. Thonke, M. Bickermann, R. M. F., and R. Goldhahn, (Unpublished).
[67] C. Cobet, R. Goldhahn, W. Richter, and N. Esser, Phys. Status Solidi B **246**, 1440 (2009).
[68] G. Rossbach, M. Röppischer, P. Schley, G. Gobsch, C. Werner, C. Cobet, N. Esser, A. Dadgar, M. Wieneke, A. Krost, and R. Goldhahn, Phys. Status Solidi B **247**, 1679 (2010).
[69] L. C. de Carvalho, A. Schleife, F. Fuchs, and F. Bechstedt, Appl. Phys. Lett. **97**, 232101 (2010).
[70] G. Grosso and G. Pastori Parravicini, *Solid State Physics* (Academic Press, Amsterdam, San Diego, 2000).
[71] E. Sakalauskas, O. Tuna, A. Kraus, H. Bremers, U. Rossow, C. Giesen, M. Heuken, A. Hangleiter, G. Gobsch, and R. Goldhahn, Phys. Status Solidi B **249**, 485 (2012).
[72] D. E. Aspnes, Phys. Rev. Lett. **28**, 168 (1972).
[73] G. Rossbach, M. Feneberg, M. Röppischer, C. Werner, N. Esser, C. Cobet, T. Meisch, K. Thonke, A. Dadgar, B. J., A. Krost, and G. R., Phys. Rev. B **83**, 195202 (2011).
[74] A. V. Rondina, M. Dietrich, A. Göldner, L. Eckey, A. Hoffman, A. L. Efros, M. Rosen, and B. K. Meyer, Phys. Rev. B **64**, 115204 (2001).
[75] P. Schley, R. Goldhahn, G. Gobsch, M. Feneberg, K. Thonke, X. Wang, and A. Yoshikawa, Phys. Status Solidi B **246**, 1177 (2009).
[76] S. Shokhovets, R. Goldhahn, G. Gobsch, S. Piekh, R. Lantier, A. Rizzi, V. Lebedev, and W. Richter, J. Appl. Phys **94**, 307 (2003).